

EXPERIMENTAL INVESTIGATION OF FLOW CHARACTERISTICS AND PERFORMANCE PARAMETERS OF A PODDED AFT ENGINE AIR INTAKE

HUMAN AMIRI^{a,*}, UMUT CAN KÜÇÜK^b, YIĞIT FIRAT KUŞÇU^b

^a Sivas University of Science and Technology, Faculty of Aviation and Space Sciences, Department of Aeronautical Engineering, Sivas Merkez, Türkiye

^b Turkish Aerospace Industries, Fethiye District, Havacılık Avenue No:17, 06980 Kahramankazan, Ankara, Türkiye

* corresponding author: human.amiri@sivas.edu.tr

ABSTRACT. This experimental study investigates the flow characteristics and performance parameters of a podded intake in aft-engine configuration at the aerodynamic interface plane (AIP), which is a typical configuration of a generic twin-engine regional jet aircraft. A scaled model aircraft with the port side hollow nacelle is equipped with total pressure rakes positioned exactly at the AIP to obtain the total pressure recovery and distortion. Multiple flight configurations (landing, take-off, and climb-out) with varying angle of attack (AoA) and side slip angle (SSA) are considered; attention has been paid to those with undesirable effects to the flow approaching the engine, by deploying flaps, slats, spoilers, and landing gear compartment. The mass flow rate and thus the mach number at the AIP is adjusted by changing the size of the exhaust nozzle. The Reynolds number dissimilarity is partially compensated by transition band application on the fuselage as well as engine inlet.

KEYWORDS: Podded air intake, wind tunnel testing, regional jet aircraft, aerodynamic interface plane.

1. INTRODUCTION

Podded air intake systems are used in aircrafts to improve the efficiency of the engine by supplying a smoother, minimally disturbed flow of air into the engine. In fact, these types of air inlets are known to be highly compatible with the engine because the distance between the intake duct and the first stage of rotary blades, whether it is a fan or a compressor, is the shortest. A proper inlet lip and diffuser shape ensures a high performance of the intake, although another major contribution is from the lip, especially at high incidence angles [1]. The quality of the air delivered by the lip to the diffuser and then to the engine is evaluated at the AIP, an imaginary plane which is located exactly at the leading edge of the fan or first stage compressor blades of a typical jet engine. Inlet distortion is governed by the operating as well as stall and surge characteristics of a turbine engine, and also vibration tests provided by federal aviation administration (FAA) regulations [2]. Typical metrics to evaluate the delivered flow quality are the total pressure recovery and its distortion of AIP [3]. The total pressure recovery of podded air intakes is inherently very high because of the shortest and straightest distance possible to the engine. Additionally, with the help of the distance from the fuselage created by pods, the low momentum boundary layer is avoided to enter the intake, and therefore the flow is minimally distorted at the AIP. Distortion levels above the maximum allowable limit are particularly harmful to fans and compressors where stall can occur. These

are unlikely to happen during a steady cruise flight of a jet aircraft. However, this ideal condition can never be maintained throughout the entire flight envelope. During the take-off and landing, there exists lots of ground effects imposing asymmetry of the flow entering the intake. In addition to that, gusts as an unsteady perturbation, and flight at side slip angle, which sometimes takes longer intervals and can be thought of as both steady and unsteady phenomena, are some examples that would take the engine to off-design conditions. One source that affects the air intake performance is crosswind. On the upwind side of the inlet, the crosswind component increases the airflow at the lip, causing further local over-speed. On top of these, the major problem of such a type of inlets is reported to be the flow separation [4]. Under these circumstances, it is mandatory to revisit the performance characteristics of the intake.

The effect of lip separated flow has been experimentally studied by Hodder [5] in GE-TF34 turbofan engine. Similar numerical work is performed by Kennedy et. al. [1] at high incidence angles. In a hybrid experimental and numerical study, Sutrisno et. al. [6] have evaluated the effect of aerodynamic surfaces (canard in this case) on the vortex dynamics of the flow entering the engine. Of course, in this case, the air intake is integrated into the body. In another study, the effect of AoA and SSA has been numerically investigated for a military aircraft equipped with an S-type inlet [7]. The authors have shown that the flight attitudes induce non-uniformities on both the temperature and the total pressure distribution at

AIP. For aft engine aircrafts, the intake is normally imposed to a thicker boundary layer, therefore arranging a podded configuration to divert this boundary layer is inevitable. To the author’s knowledge, the effect of the aircraft configuration has not yet been tested on a scaled model of aft podded jet aircraft where the engines are usually affected by the wake of the wings and control surfaces. This configuration (podded air inlet installed on the aft compartment of the aircraft) is typical to regional jets. Some examples of this type are DC-9, MD-80, Gates Learjet 25, Fokker F-28, Cessna 550, Bombardier CRJ and global series, and Tu-334. A 3-view of a typical aircraft is shown in Figure 1.

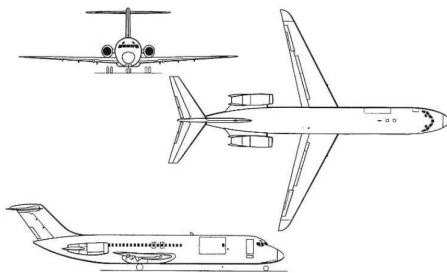


FIGURE 1. Aft podded twin engine regional jet aircraft (DC-93) [8].

The objective of this experimental study is to evaluate the performance of a podded air intake, which is quantified by total pressure recovery and its circumferential and radial distortion over the AIP. The sensitivity of the above-mentioned parameters on the mass flow rate is studied as well. Due to the lack of facilities to provide the control of mass flow through the suction or any other active methods, the mass flow passing through the nacelle is passively adjusted by changing the size of the exhaust section. To take into account the Reynolds dissimilarity, transition bands are applied on the model and wing as well as the air intake inner lips. In the Section 2, the experimental setup, different test configurations, as well as details of data acquisition, processing, and analysis are given. In the Section 3, the effect of transition strip addition and mass flow rate change are presented. The critical distortion regions in terms of AoA and SSA are found and extreme performance indices are compared for different configurations of flaps, leading edge slats, spoilers, and landing gear compartment. Finally, observations and results are summarised in the Section 4.

1.1. AIR INTAKE PERFORMANCE

Inlet flow performance indicators, which are analysed in this study, are as follows:

- a) Total pressure recovery,
- b) total pressure distortion,

c) mass flow ratio.

A summary of each indicator is given for the reader to get familiarised with the subject.

1.1.1. AREA WEIGHTED PRESSURE RECOVERY (AWPR)

Radial and circumferential position of each probe is adjusted to be at the centres of equi-areas, which allows a simplification of the area weighted intake pressure recovery as follows:

$$AWPR = \frac{P_{avg}}{P_{AIP}} = \frac{\sum_{i=1}^n P_i \cdot S_i}{P_{AIP} \cdot A} = \frac{\sum P_i}{P_{AIP} \cdot n}, \quad (1)$$

where P_{avg} is the Area weighted total pressure of each rake (shown in Figure 2) and P_{AIP} is the Total pressure over AIP. In addition to total pressure recovery, its distribution over the AIP is of an equal concern. Among the aeronautical engineers, this metric is known as total pressure distortion and is expressed either circumferentially or radially.

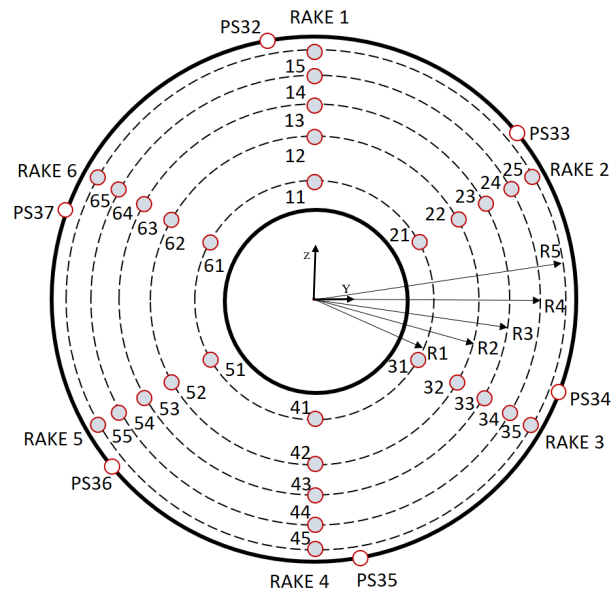


FIGURE 2. Sematics of the port side engine instrumented with 30 total and 6 static pressure tubes.

1.1.2. DISTORTION INDEX: DC60 AND DC60P

There are plenty of aerodynamic aspects that can lead to flow distortion among which is the ingestion of boundary layer [9], vortex ingestion [10], secondary internal flows [11], separation at the intake lip [12], and shock induced separation [13]. In this context, the distortion in total pressure at the AIP is considered [14] and is calculated based on the guidelines of Society of Automotive Engineers (SAE) [15]. In civil aircrafts, a high angle of incidence (AoA or SSA) can develop separation on the lips and subsequently decrease the total pressure in the separated zone on the AIP [16]. It has previously been discovered that the propulsion

system efficiency is affected by the inlet total pressure distortion. Results from a ground testing facility test of a turbofan engine with a circumferential inlet distortion pattern revealed a 2% loss in gross thrust and a 6% increase in specific fuel consumption (SFC) [17].

DC60 represents the difference in pressure between the lowest mean total pressure over a 60° sector (P_{60}) and the area weight total pressure (P_{avg}). The difference is then divided by the dynamic pressure at engine face.

$$DC60 = \frac{P_{60} - P_{avg}}{q_{avg}}, \quad (2)$$

where q_{avg} is the dynamic pressure at the engine face and P_{avg} is the average of all total pressure readings as shown in *AWPR* equation in the definition of total pressure recovery. As the rakes used in the experiment are 60° apart, P_{60} can be equated to the weighted average of total pressures on the rake that yields the lowest average total pressure. While this rake is named as P_{rake_i} , its two neighbor rakes can be labelled as $P_{rake_{i-1}}$ and $P_{rake_{i+1}}$, respectively. Then, the weighted average of these rakes is:

$$P_{60} = 0.25 \times P_{rake_{i-1}} + 0.5 \times P_{rake_i} + 0.25 \times P_{rake_{i+1}}. \quad (3)$$

1.1.3. MASS FLOW RATE

The following formula gives the absolute mass flow rate of air passing through the AIP considering the compressibility of the flow.

$$MFR = \frac{A \cdot P_t}{\sqrt{T_t}} \cdot \sqrt{\frac{\gamma}{R} \cdot M_{AIP} \left(1 + \frac{\gamma-1}{2} M_{AIP}^2\right)^{\frac{-\gamma-1}{2(\gamma-1)}}}, \quad (4)$$

where A is the AIP total area and T_t is the total temperature which is considered to be constant assuming adiabatic flow. γ and R values are well known gas (air) constants. The mach number at AIP plane is obtained from isentropic relation,

$$\left(\frac{P_t}{P_s}\right) = \left(1 + \frac{\gamma-1}{2} M^2\right)^{\frac{\gamma}{\gamma-1}} \rightarrow M_{AIP} = \sqrt{\frac{2}{\gamma-1} \left[\left(\frac{P_t}{P_s}\right)^{\frac{\gamma-1}{\gamma}} - 1\right]}, \quad (5)$$

where P_0 and P_S are the area weighted total pressure at the AIP (nacelle) rakes and average of the nacelle static pressures located on the inner surface, respectively.

The corrected mass flow rate value is given by the following formula and is used throughout the report.

$$MFRC = MFR \cdot \sqrt{\frac{\theta}{\delta}}, \quad \text{where} \quad (6)$$

$$\theta = \frac{T_t}{T_{ref}} \quad \text{and} \quad \delta = \frac{P_t}{P_{ref}}.$$

Reference temperature and pressure values are $T_{ref} = 288.15$ K and $P_{ref} = 101\,325$ Pa, respectively.

2. MATERIALS AND METHODS

2.1. WIND TUNNEL FACILITY

The experiment is performed in a low subsonic closed loop wind tunnel with atmospheric closed test section. The test section is 6.1 m long and has a cross section of 3.05 m (width) by 2.44 m (height). It is equipped with chamfered divergent corners to reduce the effects of corner vortices. The maximum attainable speed inside the empty test section is 80 m s^{-1} (288 km hr^{-1}) with axial and total turbulence intensities of 0.15% and 0.62%, respectively [18].

2.2. REGIONAL JET AIRCRAFT MODEL AND PRESSURE MEASUREMENT INSTRUMENTATION

In order to evaluate the flow at the AIP of a generic regional jet, specifically, to find the off-design performance of the intake at several AoA and SSA, a typical regional jet obtained from [19] with two aft body podded turbofan engines has been chosen and built in scale 1 : 15. This scale is chosen according to the maximum wet area blockage of the model as well as the length limitations according to the test section size. The blockage is almost 7% with respect to the model gross wing area, 65% along the span, and 33% with respect to the model overall length. The free-stream mach number of 0.2 is automatically maintained by the wind tunnel control system throughout the entire measurements. This is almost the maximum achievable speed for this facility, with respect to the above mentioned blockage values. The full span model structure is supported by a single sting connected to the tail cone of the aircraft. This ensures minimum disturbances to the airflow and reduces aerodynamic effects on the model. The sting mechanism is able to change the pitch as well as roll angles of the model, while the yaw angle can be adjusted through a rotating table on which the sting apparatus is fixed over the wind tunnelrefs bottom wall. The AoA and SSA of the model are controlled by pitch and yaw angles of the mentioned mechanism, respectively. Figure 3 shows the schematics of the sting connected to the model aircraft.

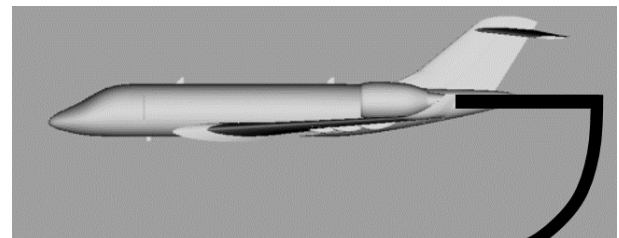


FIGURE 3. Schematics of the sting connected to the tail of the model.

Both nacelles are made hollow (through flow engines) while only the port side nacelle is equipped with equal area distributed total pressure probes, every 5° of which are installed on a rake as shown schematically

in Figure 2. The pressure rake is known to be a well-established industrial technique to measure the distortion at the engine's AIP [17]. As mentioned above, the distribution of the points is selected so that they are positioned at the centroid of equal area sections over the circular AIP, so that the obtained pressure recovery values obtained are inherently area averaged. The number of pressure rakes in a jet engine's nacelle, conventionally set at 40, significantly influences the measurement accuracy. Increasing the pressure tubes improves spatial resolution for a more detailed total pressure distribution but introduces blockage effects, demanding a careful mitigation. Conversely, reducing the number simplifies the setup and minimises blockage but sacrifices spatial resolution. The optimal choice hinges on balancing the enhanced accuracy with the potential blockage impact, emphasizing the need for meticulous optimisation based on specific aerodynamic considerations within the nacelle.

In addition, the surface static pressure is measured at 6 ports placed on the interior wall of the air inlet on the AIP circumference. These ports (PS32 through PS37) are also visible in Figure 2. The numbering of the total pressure probes is done with two digits, corresponding to the rake number (1 through 6) and ring number (1 through 5), respectively.

All total and static pressure ports are connected through tubes to a digital differential pressure scanner, which is embedded inside the aircraft model in order to reduce the errors of long tubing on pressure readings. A pressure scanner (Scanivalve – MPS 4264) with 64 ports, which can measure differential pressures up to ± 1 psi with a sensitivity of 0.06% (i.e., about 8 Pa), is used. To obtain the absolute pressure value at each port, the atmospheric pressure is supplied to the other end of the pressure transducer and its value is being measured with a SETRA 2270 absolute pressure sensor. Temperature is measured with two k-type thermocouples at the front and back of the test section. The aircraft model is connected to a sting that is electronically controlled to maintain the aircraft attitude (AoA and SSA). These angles are measured with a Wyler Clinotronic sensor, which can measure angles of up to $\pm 45^\circ$ with very high sensitivity (max error is about 0.033°). The data are then transferred to a PC to be recorded and analysed.

In order to change the mass flow rate passing through the engine, in addition to the normal exhaust with a convergent shape, another nozzle is designed with a large cross sectional area to pass more air through the nacelle. This way, two different mass flow rates inside the nacelle can be realised. It has been shown before that when there is an incompressible flow inside a duct, its quantity (i.e. mass flow rate) is determined primarily by the duct exit area. In other words, there is no dependency between the mass flow rate and the inlet area of the duct [4]. The small and large nozzles are depicted in Figure 4.

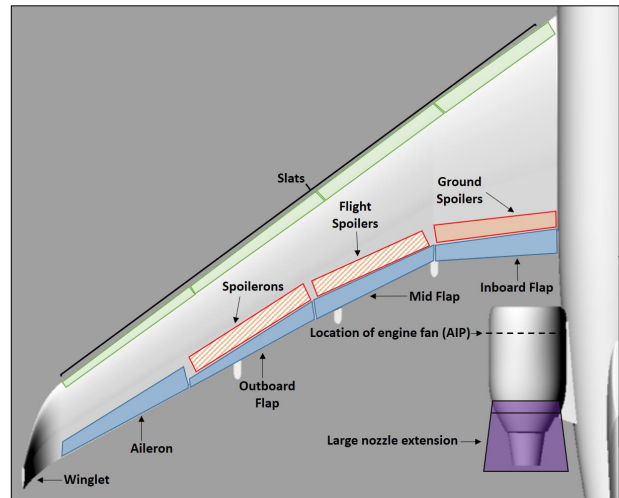


FIGURE 4. Control surfaces on the main wing of model aircraft; normal (small) nozzle and the extended (large) nozzle attached to the nacelle exhaust.

2.3. CONFIGURATION LIST (FLIGHT CONDITIONS)

The configuration list, which is given in Table 1, is prepared considering various flight conditions that might impose an undesirable flow into the air inlet. In this table, MFS refers to “multi-function spoilers” where “multi” indicates that spoilers can be used as ailerons as well. These are shown in Figure 4 (flight spoilers and spoilerons) and Δ MFS being its deflection angle, Δ slat being the leading-edge slats deflection, Δ flap being the trailing edge flaps deflection, and LG is the landing gear position. Two different nozzles are tested in this set of experiments, small and large, representing low and high mass flow rates passing through the nacelle compartment, respectively. The free stream velocity is fixed at $M = 0.2$ by the wind tunnel control system. Different combinations of AoA [-9° to 17°] and SSA [0° to 22°] in pitch-pause scenarios are considered at each configuration listed in Table 1.

2.4. DATA ACQUISITION, PROCESSING, AND ANALYSIS

It is a matter of concern to find the appropriate dwell time (time to wait before sampling the data after setting each desired position in pitch-pause mode), data acquisition time (time to record the data), and data sampling frequency. Measured pressure values along with other measured data (temperature, angles, etc.) are processed within the internal data acquisition system of the tunnel facility and time-averaged values of the data are provided for each of the rake and surface static pressure ports. After testing a set of dwell times [2, 4, 8, and 16 seconds], data acquisition time [5, 10, 15, 20, 25, and 30 seconds], and sampling frequencies [50, 300, and 500 Hz], it was decided to choose the following values for the entire measurements: 8 seconds for dwell time, 20 seconds to acquire data with a

Config.	Flight condition	Configuration properties	Δslat°	Δflap°	ΔMFS°	LG	Nozzle
C1	landing	Baseline + MFS	20	30	40	Down	Large
C2	take-off	Baseline + MFS	20	16	40	Up	Large
C3	take-off	Baseline + MFS	20	6	40	Up	Large
C4	Climb-out	Baseline + MFS	0	0	40	Up	Large
C5	Climb-out	Baseline + MFS + small nozzle	0	0	40	Up	Small

TABLE 1. Test plan configuration list.

500 Hz sampling rate. Trials were performed at nominal AoA and SSA combinations ($[0,0]$, $[10,0]$, $[-10,0]$, $[0,10]$, and $[-10,10]$) considering the AIP flow characteristics (Pressure recovery, distortion, and mass flow ratio) with repeat criteria for each parameter shown in Table 2. The values are determined on the basis of experimental experience, the accuracy of the measurement system, and the uncertainty of the data.

Variable	Percentage [%]
Distortion	0.5
Pressure recovery	0.1
Mass flow rate (MFR and MFRC)	1

TABLE 2. Repeat criteria for measured variables.

The above mentioned trials are part of wind tunnel shake-down tests on baseline model corresponding to configuration C1 in the test matrix Table 1 (Slat = 20° , flap = 30° , MFS = 40° , No aileron deflection, landing gear down, and large nozzle attached to the nacelle).

3. RESULTS AND DISCUSSION

3.1. CONTOURS OF TOTAL PRESSURE RECOVERY

Sample contour plot of pressure recovery (AWPR) is given in Figure 5. Y and Z axes are expressed in unit radius of the AIP circular plane (between -1 and $+1$) with the centre of AIP at $Y = Z = 0$ so that the tip is at radius 1. The smaller circle represents the hub, in this case at 0.35 of the unit radius. The small black dots show the exact place of the total pressure rakes and the contour plot is produced by triangulation of data at these points. A 60° sector of the AIP circle including the rake with the lowest total pressure is highlighted with a dashed red line. It is worth noting that the fuselage of the aircraft remains at the left side of the contour plots (forward looking aft).

Of the scenarios in the test matrix, those with negative SSA (i.e. when the engine is windward) are not of concern as the port (left hand side) engine is not affected by the fuselage as much as it is when the engine is leeward (the model is positively yawed); keeping in mind that the positive SSA is when the aircraft nose is yawed CCW. The minimal effect of

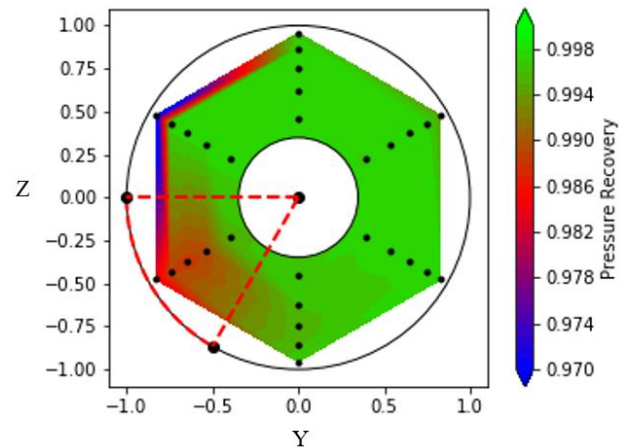


FIGURE 5. Sample contour plot of AIP total pressure recovery.

negative SSA on the port engine is depicted in Figure 6, which is a comparison of $\text{SSA} = -16^\circ$ and $+16^\circ$ with sweep in AoA. However, minor differences at positive SSA can still be detected.

3.2. TRANSITION STRIP APPLICATION

Due to the relatively low Reynolds numbers achievable with small-scale models, transition strips or trip dots are installed on the nacelle intake leading edge to simulate the full-scale laminar to turbulent boundary layer flow transition point. Motycka [20] conducted a study using JT9D engine (installed on Boeing 747 aircraft) and a scaled model to evaluate the conservativeness of distortion measurements made on scale models. He reported the sensitivity of separation AoA to the Reynolds number such that the separation AoA is higher in a higher Reynolds number during a real flight. Rather than scale effects, he also mentioned the engine/inlet coupling to be responsible for these differences. In the present study, to model the transition point, a CAD CUT[®] product trip dot with a size of 5 mil (≈ 0.0127 mm) is used for the nacelle inner surface. Transition strip calculations are performed based on the flat plate equations [21]. Transition band (trip dot) effects are examined at three different side-slip (SSA) [0° , 8° , and 16°] with sweeping AoA in the range of $[-9^\circ$ $17^\circ]$. Trip dots are added in two steps: first is to apply 7.2 mil dots to the outer surface of the model and engine, and in the second step, the

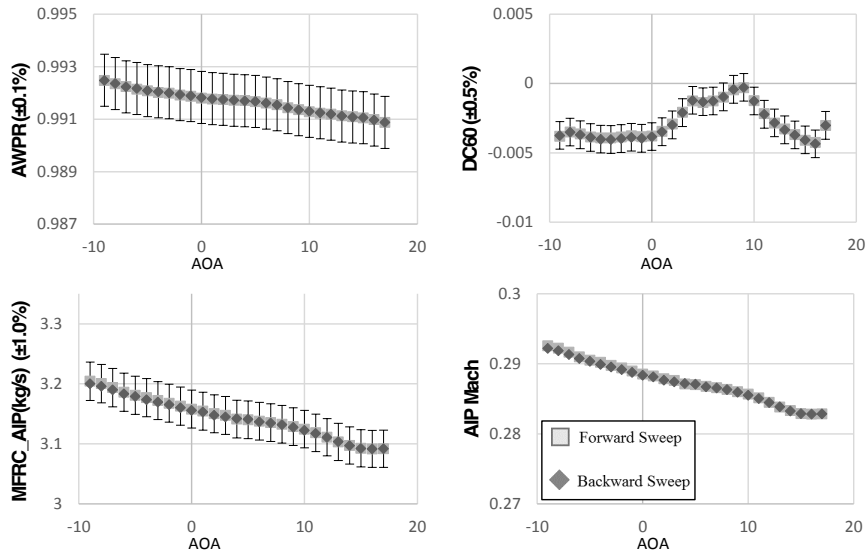


FIGURE 6. AIP metrics at negative and positive side-slip angles (SSA = -16° and $+16^\circ$) with varying AOA.

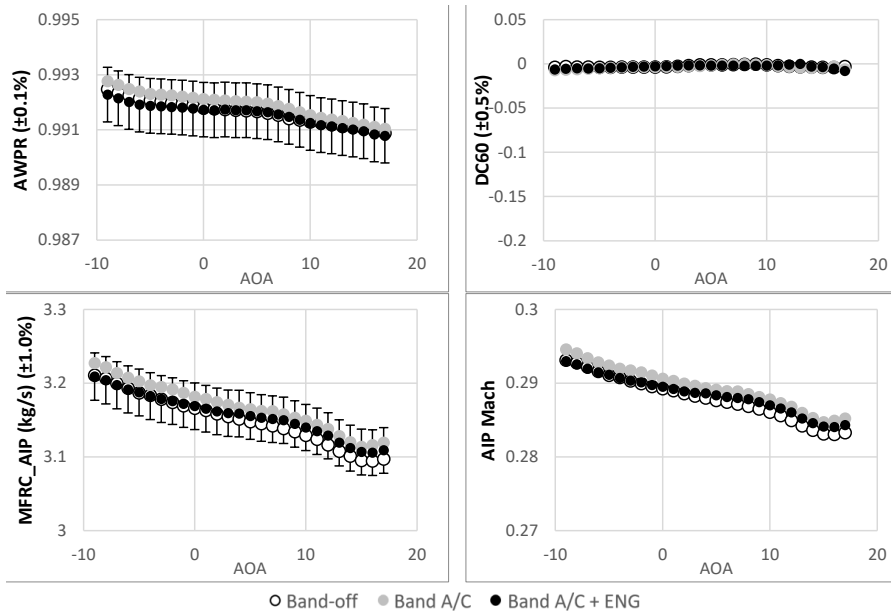


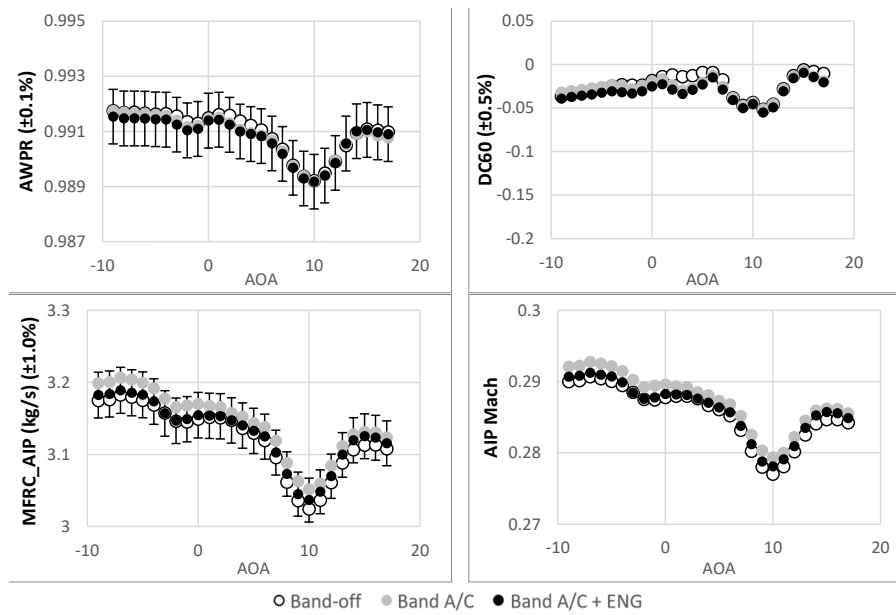
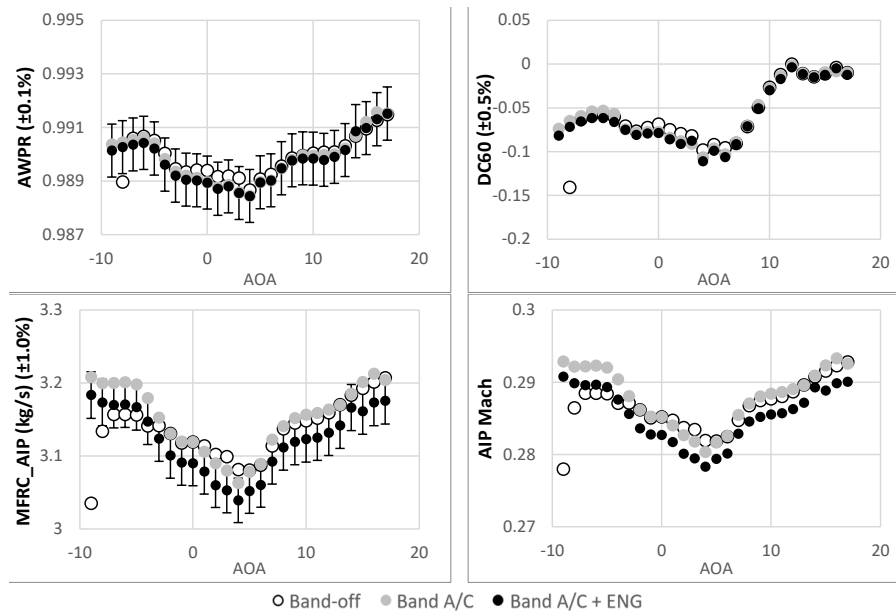
FIGURE 7. Effects of trip dot addition to the baseline model, side slip angle = 0° .

inner surface of the engine intake lip is additionally equipped with 5.0 mil dots (≈ 0.0127 mm). The outer surface transition bands (trip dots) are placed 3.5 cm downstream of the nose tip and 2.5 cm downstream of wings' leading edge. The inner trip dots are placed 1.0 cm downstream of the intake lip. The results for zero side slip angle are given in Figure 7 wherein empty circles (Band-off) refer to the condition when no transition band is applied to the model surface, grey circles (Band A/C) are for the condition that only the aircraft surface is equipped with the transition band, and black circles (Band A/C + ENG) belong to the condition when the transition band is applied on both the aircraft surface and the nacelle inner wall.

In Figure 8, the AIP metrics are compared while the

baseline model is at SSA = -8° at different angles of attack. SSA = 16° is the last case studied for the trip dot effects. The AIP metrics are depicted in Figure 9. At an extreme condition of low negative AoA (-9° and -8°), a jump in all AIP metrics in the configuration without any trip dot has been observed. This difference is significant in distortion values. Since there is no diagnostic procedure to detect the separated flow streamline, it is not possible to identify the source of this undesirable flow distortion. Prospect computational flow investigations may reveal the source of this sudden reduction in the inlet performance.

Repeatability check on the data is evaluated in one sample case. AoA is changed from -9° to 17° both in the forward and the backward sweep. Figure 10 shows that during the sweep, the intake performance

FIGURE 8. Effects of trip dot addition to the baseline model, side slip angle = 8° .FIGURE 9. Effects of trip dot addition to the baseline model, side slip angle = 16° .

parameters clearly remain inside the repeat criteria expressed in Table 2.

3.3. MASS FLOW RATE CONSIDERATIONS

The flow of air passing through the nacelle is adjusted using two differently sized nozzles. One is the typical nozzle of the model itself and the second one is a modified larger version. It is worth noting that this counts as a passive method to manipulate the mass flow rate inside a duct. Although it doesn't seem very efficient compared to the active methods such as suction, the duct exhaust area has been previously shown to be responsible for the mass flow passing through a duct for incompressible flow conditions [4]. Of course, one of the major concerns in this study is

to evaluate the air intake efficiency and its sensitivity to the inlet mass flow rate. At $SSA = 0^\circ$, the mass flow passing through the port (left) nacelle is obtained to be almost equal to 1.0 and 3.0 kg s^{-1} for small and large nozzle configurations, respectively.

When the nozzle is changed from large to small, decreasing the mass flow rate (i.e. by changing configuration from C4 to C5 (see Table 1), the values of distortion as shown in Figure 11, are consistently increasing in magnitude. Measurement points are depicted with black dots within the contour plots. For C4 configuration (climb-out with large nozzle attached to the nacelle), the distortion value is acceptable over almost the entire investigated region except at the lower limit of the AoA and very high SSA (Figure 11(a)

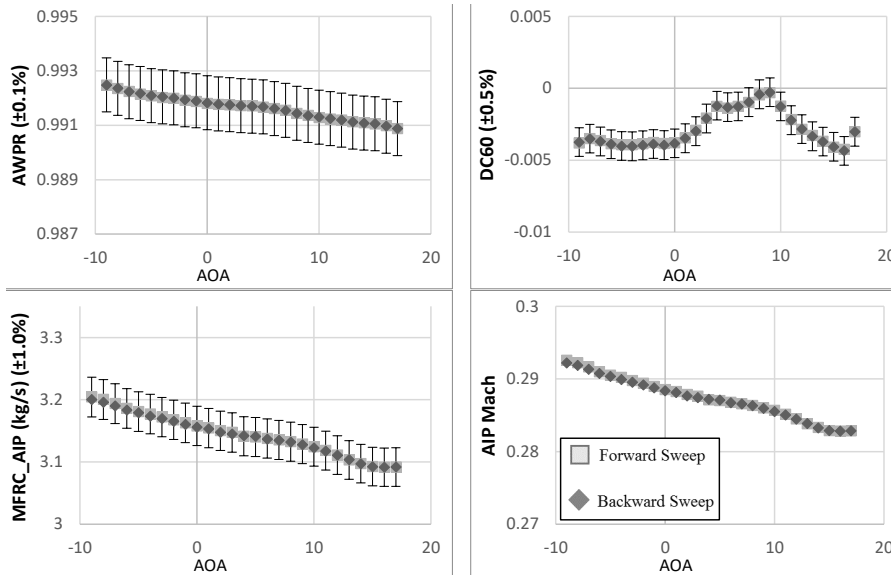


FIGURE 10. Repeatability check on AIP metrics.

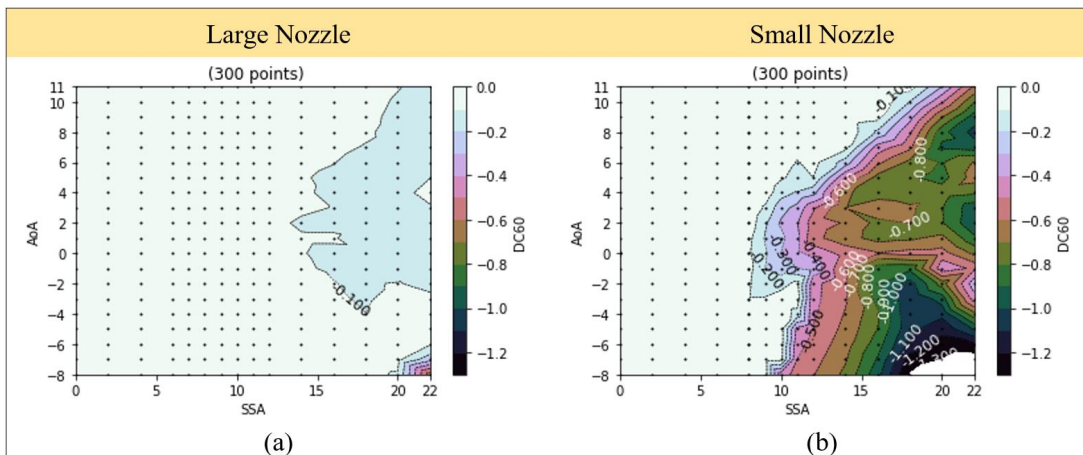


FIGURE 11. Effect of mass flow rate change on the AIP distortion, (a) large nozzle configuration, (b) small nozzle configuration.

bottom right corner). By switching the nozzle (C5 configuration shown in Figure 11(b)), it is clear that the distortion exceedances occupy wider ranges in the tested flight region. Since the scale of the two figures are equalised, there is a clipped region at the bottom right of Figure 11(b), showing the higher distortion magnitudes at corresponding flight attitudes.

The effect of mass flow rate on the pressure recovery is minimal (see Figure 12) since the magnitude of AWPR is not dropping below 0.98 in most cases, except at very high side slip angles. A simultaneous analysis of total pressure recovery values of these configurations (Figure 12) reveals that there should not be a very significant difference between the pressure distributions, although the obtained values of DC60 contradict this fact. As will be shown shortly, this inconsistency arises from the dynamic pressure term in the definition of DC60 metric. Here, to conclude the overall performance, the highest distortion, as anticipated, happens at the high cross wind (high SSA)

and nose down (negative AoA) conditions.

3.4. GEOMETRIC CONFIGURATION EFFECTS (FLAPS, SLATS AND ETC.)

As mentioned before, the effect of geometric configuration is significant for an aft-podded jet aircraft since engines are usually affected by the wake of wings and deflected control surfaces. The current set of experiments were conducted with 5 different configurations that geometrically represent different flight conditions as given in Table 1. In this manner, the effects of different control surfaces can be determined by comparing the corresponding configurations and their extremum metrics, which are summarized in Figure 13.

The flap angle effect can be determined via comparing C2 and C3 configurations, for which the only difference is that C2 has more deflected flaps, 16° compared to 6° as in C3 configuration. As given in Figure 13, C3 configuration has a lower maximum

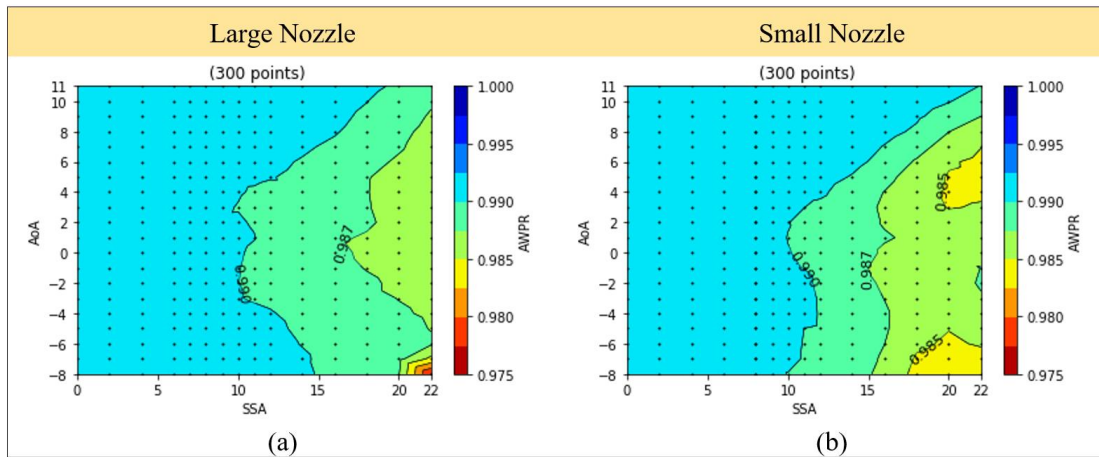


FIGURE 12. Effect of mass flow rate change on the area weighted pressure recovery, (a) large nozzle configuration, (b) small nozzle configuration.

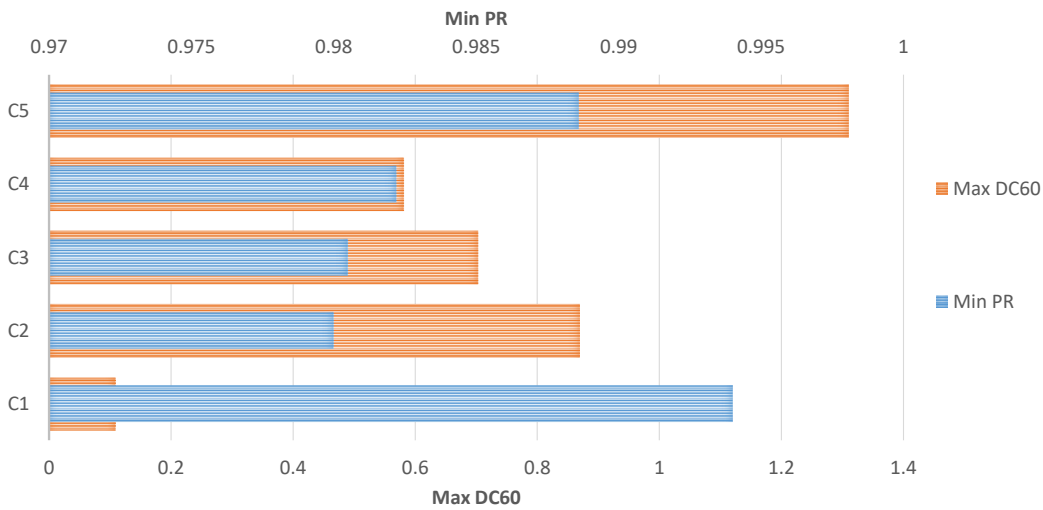


FIGURE 13. Extreme performance index comparison for different flight configurations.

DC60 and a higher minimum AWPR as compared to C2. Therefore, it can be concluded that increased flap deflection angle decreases both the overall performance and stability. It has to be noted that this comparison is only valid for C2 and C3 cases and does not apply for the other flight conditions. This is expected, as increasing the flap angle generates more blockage to the free stream flow and amplifying vortex shedding and downwash. As a result, the engine is exposed to more deviated and degraded flow as vortex ingestion to the engine is increased.

The combined flap and slat deflection angle effect is determined by comparing C3 and C4 configurations as the only differences are slat and flap deflection angles, remembering that C4 configuration has non-deflected flaps and slats. In this comparison, both the overall performance and stability decrease similarly with increased slat and flap angle as the maximum DC60 is lower and minimum AWPR is higher for the C4 (non-deflected) configuration. Again, this is an expected result due to the similar aforementioned phenomena associated with flap and slat deflections.

3.5. TOTAL PRESSURE DISTORTION

It is found that there is a significant difference in critical distortion zones between the small and large nozzle conditions (C4 and C5 configurations). The contours of pressure recovery of two sample cases (C5 and C4) are shown in Figure 14. It is evident that the total pressure drop is more critical in large nozzle case as it is shown by AWPR as well. Although DC60 is considered high in both conditions, the distortion value for small nozzle - which is expected to be smaller in magnitude - is significantly larger. The argument starts with the definition of DC60, which is calculated based on the dynamic pressure at the engine face (q_{avg}) (see distortion index: DC60 and DC60P). q_{avg} values for the mentioned cases are also given below each contour. It is evident that the q_{avg} for the small nozzle is 5 times smaller than that of the large nozzle. This is the reason of obtaining considerable artificial high distortion due to the very low dynamic head for the small nozzle configuration.

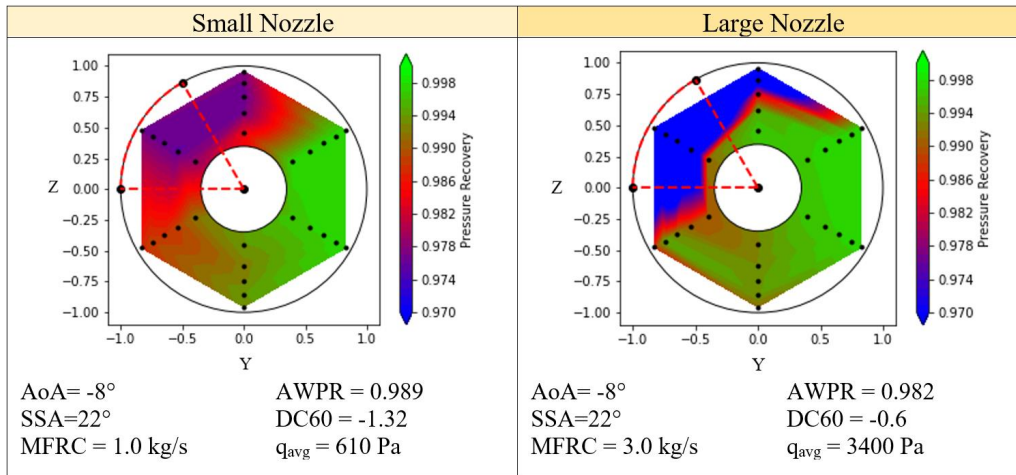


FIGURE 14. Comparison of total pressure distribution between Small and Large nozzle configurations of similar cases (-8° AOA, $+22^\circ$ SSA) of Green model.

4. CONCLUSIONS

In the tests described in this paper, different flight configurations of an aft podded twin-jet engine aircraft model are investigated. The subject of flight surface configurations has been never touched in open literature before, at least for a civil transport aircraft. In this study, the total pressure values on AIP of the left (port) engine were measured over 30 points distributed over an array of 6 by 5. The static pressure on the AIP is also measured at 6 corresponding points on the inner wall of the nacelle with an appropriate offset to the total ports to avoid any interference.

The particular aim of this experimental study is to assess the performance of a podded air intake that is installed on the aft compartment of an aircraft. Examples of such a configuration can be found in typical regional jets. The total pressure recovery and its circumferential distortion over AIP are analysed with respect to each flight configuration and the aircraft attitude (angle of attack and side slip angle). The flight configurations (and thus different aircraft configurations, such as landing gear, wing slats and flaps, ailerons, and spoilers) are believed to interact with the engine/intake stream tube. To take into account the Reynolds dissimilarity, transition bands are applied on the model and wing as well as the air intake inner lips. In addition, two different mass flow rates passing through the engine are adjusted by alternating the rear exhaust nozzle and compared to determine the mass flow rate sensitivity to performance and distortion metrics. Observations and results are given below, together with some suggestions for future work.

- Distortion index (DC60) generally remains low, except at very high SSA and negative AoA. The only exception to this is when the exhaust nozzle is changed from large to small (forcing the engine to operate at too low mass flow rates) and this is discussed in detail in the context.
- The minimum area weighted pressure recovery

(AWPR) is found in the C2 configuration with a value of 0.98. This corresponds to the rolling take-off condition with fully open slats and flaps, while the spoilers are also deflected to a maximum angle of 40° . This high-pressure recovery is the inherent characteristic of straight round air intakes.

- The maximum flow distortion (DC60) on AIP is observed in the C5 configuration, corresponding to a small nozzle and only MFS deflected at 40° .
- The mass flow passing through the port (left) nacelle equipped with a large nozzle is obtained to be almost 3 times that of a small (original) nozzle. As it is discussed in the context, a significant difference of dynamic pressure at the fan face between the large and small nozzle configurations introduces an abrupt change in the extension of critical distortion zones. Such that, for the small nozzle configuration, the low value of dynamic pressure at the AIP has led to unrealistic DC60 values that contradict with the distribution of corresponding pressure recoveries. Therefore, DC60 metric should not be the only parameter to rely on for the evaluation of total pressure distortion on AIP. This issue is more profound in wind tunnel experiments with scaled models and in cases where there is no dynamic similarity in Reynolds numbers.
- Minimum AWPR and Maximum DC60 at different configurations are summarised in Figure 13.
- This experiment was originally proposed to perform a study on the AIP performance metrics of an aft-podded engine aircraft model, and therefore only one nacelle (port side) is equipped with the total pressure rakes and static pressure ports. However, the addition of second instrumentation on the starboard engine would have significantly improved the value and accuracy of the pressure measurements at a small additional cost.
- Obviously, the mass flow rate of the air passing

through the nacelle under investigation differs significantly from that encountered in actual flight operations. Existing literature explores the use of air ejectors to emulate a more representative flow within the nacelle. However, the scope of this study extends beyond the specific flow characteristics at the Aerodynamic Interface Plane and encompasses data pertaining to the external aerodynamics of the aircraft. Consequently, the necessity to consider both aspects has led to the decision to forego the implementation of elaborate ejectors or electric fans as a cost-saving measure within the constraints of the allocated budget.

- As mentioned in the context, the confidence in the data for a scaled model is shown to be strongly dependent on the Reynolds number similarity and engine/inlet coupling. Although the pressure rake produces a blockage inside the nacelle to somewhat resemble the engine compartment in a real case, it is still non-rotating and the whole effect of the rotating engine on the inlet flow cannot be entirely simulated. This can be investigated more thoroughly with the use of CFD in future studies.

ACKNOWLEDGEMENTS

Authors would like to acknowledge the Turkish Aerospace Industries (TAI) and Ankara wind tunnel (ART) facility for their contribution and cooperation.

LIST OF SYMBOLS

Acronyms

AIP Aerodynamic Interface Plane
 AoA Angle of Attack [°]
 AWPR Area Weighted Pressure Recovery
 CAD Computer Aided Design
 CCW Counter clock-wise
 DC60/DC60P Total Pressure distortion over 60° sectors on AIP
 FAA Federal Aviation Administration
 LG Landing Gear
 MFR Mass flow rate [kg s⁻¹]
 MFRC Corrected Mass Flow Rate [kg s⁻¹]
 MFS Multi-function Spoiler
 PS Static pressure port on the model
 SAE Society of Automotive Engineers
 SFC Specific Fuel Consumption

Roman symbols

A Net flow area of AIP (engine face) [m²]
 M Mach number [-]
 P Pressure [Pa]
 P_{60} Weighted average of total pressures on the rake with the lowest average total pressure and its two neighbour rakes [Pa]
 P_{AIP} Total pressure over AIP [Pa]
 P_{avg} Area weighted total pressure of each rake [Pa]
 P_i Total pressure of each individual pitot probe [Pa]

$P_{rake,i}$ Total Pressure of the rake with lowest average total pressure [Pa]
 P_{ref} Pressure reference (101 325 Pa) [Pa]
 R Gas constant [kJ/kgK]
 S Static value [-]
 T Temperature [K]
 T_{ref} Temperature reference (288.15 K) [K]
 i Pressure rake number [-]
 n Number of pitot probes [-]
 q_{avg} Dynamic pressure at AIP (engine face) [Pa]
 ref Reference value [-]
 s Covered area by each individual pitot probe [m²]
 t Total (stagnation) value [-]

Greek symbols

Δ Deflection angle [°]
 ΔMFS Deflection in multi-function spoilers [°]
 $\Delta slat$ Deflection in slats [°]
 $\Delta flap$ Deflection in flaps [°]
 γ Ratio of the specific heats (1.4 for air) [°]
 δ Pressure ratio (P_t/P_{ref})
 θ Temperature ratio (T_t/T_{ref})

REFERENCES

- [1] S. Kennedy, T. Robinson, S. Spence, J. Richardson. Computational Investigation of Inlet Distortion at High Angles of Attack. *Journal of Aircraft* **51**(2):361–376, 2014. <https://doi.org/10.2514/1.C031789>
- [2] ECFR. 27.939 Turbine Engine Operating Characteristics, National archives and records administration, 1976.
- [3] J. Pečinka, G. T. Bugajski, P. Kmoč, A. Jílek. Jet engine inlet distortion screen and descriptor evaluation. *Acta Polytechnica* **57**(1):22–31, 2017. <https://doi.org/10.14311/AP.2017.57.0022>
- [4] J. Seddon, E. L. Goldsmith. *Intake aerodynamics*. American Institute of Aeronautics and Astronautics, 2nd edn., 1999.
- [5] B. Hodder, B. Farquhar, M. Dudley. A large-scale investigation of engine influence on inlet performance at angle-of-attack. In *1st Flight Test Conference*. American Institute of Aeronautics and Astronautics, 1981. <https://doi.org/10.2514/6.1981-2481>
- [6] Sutrisno, T. A. Rohmat, S. B. Wibowo, S. Iswahyudi. Vortex dynamics study of the canard deflection angles' influence on the Sukhoi Su-30-like model to improve stall delays at high AoA. *Aerospace* **6**(2):12, 2019. <https://doi.org/10.3390/aerospace6020012>
- [7] T. Triantafyllou, T. Nikolaidis, M. Diakostefanis, P. Pilidis. Total pressure distortion levels at the aerodynamic interface plane of a military aircraft. *The Aeronautical Journal* **119**(1219):1147–1166, 2015. <https://doi.org/10.1017/S0001924000011179>
- [8] Skybrary.aero. [2021-07-10]. <https://www.skybrary.aero>.

- [9] D. K. Hall, E. M. Greitzer, A. Uranga, et al. Inlet flow distortion in an advanced civil transport boundary layer ingesting engine installation. *Journal of Turbomachinery* **144**(10):101002, 2022. <https://doi.org/10.1115/1.4054035>
- [10] T. Berthelon, A. Dugeai, J. Langridge, F. Thouverez. Analysis of vortex ingestion impact on the dynamic response of the fan in resonance condition. In *Volume 7A: Structures and Dynamics*. American Society of Mechanical Engineers, 2019. <https://doi.org/10.1115/GT2019-90939>
- [11] W. T. Cousins. History, philosophy, physics, and future directions of aircraft propulsion system/inlet integration. In *Volume 2: Turbo Expo 2004*. ASMEDC, 2004. <https://doi.org/10.1115/GT2004-54210>
- [12] M. Davis, A. Hale, D. Beale. An argument for enhancement of the current inlet distortion ground test practice for aircraft gas turbine engines. *Journal of Turbomachinery* **124**(2):235–241, 2002. <https://doi.org/10.1115/1.1451087>
- [13] S-16 Turbine Engine Inlet Flow Distortion Committee. An Assessment of Planar Waves, 2021. <https://doi.org/10.4271/AIR5866A>
- [14] S-16 Turbine Engine Inlet Flow Distortion Committee. Inlet Total-Pressure-Distortion Considerations for Gas-Turbine Engines, 2017. <https://doi.org/10.4271/AIR1419C>
- [15] Society of Automotive Engineers (SAE). Gas Turbine Engine Inlet Flow Distortion Guidelines, SAE ARP1420, 2002.
- [16] U. Doll, M. Migliorini, J. Baikie, et al. Non-intrusive flow diagnostics for unsteady inlet flow distortion measurements in novel aircraft architectures. *Progress in Aerospace Sciences* **130**:100810, 2022. <https://doi.org/10.1016/j.paerosci.2022.100810>
- [17] S-16 Turbine Engine Inlet Flow Distortion Committee. Gas Turbine Engine Inlet Flow Distortion Guidelines, 1978. <https://doi.org/10.4271/ARP1420>
- [18] Ankara Wind Tunnel. [2021-07-10]. <https://www.art.gov.tr>.
- [19] GrabCAD. [2021-07-10]. <https://www.grabcad.com>.
- [20] D. Motycka, S. Welling, F. Lewis-Smith. Comparison of model and full scale inlet distortions for subsonic commercial transport inlets. In *Aircraft Design Systems and Operations Meeting*. American Institute of Aeronautics and Astronautics, 1984. <https://doi.org/10.2514/6.1984-2487>
- [21] J. B. Barlow, W. H. Rae, A. Pope. *Low-speed wind tunnel testing*. John Wiley & Sons, 3rd edn., 1999.